Review article

Check for updates

Emerging memory electronics for non-volatile radiofrequency switching technologies

Dahyeon Kim [1,6], Sung Jin Yang [2,6], Nicolás Wainstein [3,4], Simon Skrzypczak[5], Guillaume Ducournau[5], Emiliano Pallecchi[5], Henri Happy[5], Eilam Yalon [3], Myungsoo Kim[1] ✉ & Deji Akinwande [2] ✉

Abstract

Radiofrequency (RF) switches are pervasive in modern communication and connectivity systems such as cellular networks, satellite communications and radar systems. Contemporary systems typically use transistor RF switches; however, owing to the growing demand for devices with high speeds, reliability and energy efficiency, research into alternative materials and devices, particularly those based on non-volatile switching physics, is expanding. In this Review, we discuss recent advances in RF switches based on emerging and two-dimensional (2D) materials. Following an overview of RF switches based on emerging memory technology, such as random-access memory, conductive-bridge random-access memory and phase-change memory, we describe 2D non-volatile RF switch technologies, including device fabrication, high-frequency performance, switching time, power handling, electromagnetic and thermal studies. We then highlight integration of silicon complementary metal–oxide–semiconductors with various switch applications in connectivity circuits. Finally, we outline possible directions for future research such as sixth-generation (6G) networks with low latency and high bandwidth for augmented reality and virtual reality.

Sections

[1]Department of Electrical and Computer Engineering, Ulsan National Institute of Science and Technology (UNIST), Ulsan, South Korea. [2]Microelectronics Research Center, The University of Texas at Austin, Austin, TX, USA. [3]Technion, Israel Institute of Technology, Haifa, Israel. [4]Intel Corporation, Haifa, Israel. [5]IEMN, University of Lille, CNRS UMR8520, Villeneuve d'Ascq, France. [6]These authors contributed equally: Dahyeon Kim, Sung Jin Yang. ✉e-mail: myungsookim@unist.ac.kr; deji@ece.utexas.edu

Review article

Key points

- An RF switch is a device that controls radiofrequency signals, allowing multiple signals to be selected or connecting or disconnecting a signal from a circuit.

- High-performance RF switches can provide reconfigurability in RF front-end systems, which increases design flexibility and reduces costs.

- Unlike conventional RF switches, non-volatile RF switches can operate without an external static power supply because of their non-volatile resistive switching (NVRS) effect.

- NVRS 2D RF switches are promising candidates that can play a key role in next-generation data communication technologies such as 6G and satellite communications, which are expected to offer considerably higher speeds, lower latency and energy efficiency.

Introduction

The increasing complexity of radiofrequency (RF) standards for mobile communication systems, such as 5G and 6G, is driving the demand for high-performance RF front-end solutions that meet the following criteria: wide bandwidth, low power consumption, high power transmission and linearity[1–4]. The RF front end is the part of a radio receiver or transmitter that receives and transmits radio signals. It consists of many components, including antennas, low-noise amplifiers (LNA), power amplifiers, mixers, filters and RF switches (Fig. 1a). RF switches are used to route signals between different blocks, such as amplifiers, mixers and filters, and to enable the use of multiple frequencies[5–18], making them essential components in mobile communication and reconfigurable radio systems, Internet of Things, and phased-array networks. In the simplest model of an RF switch (Fig. 1b), it can be represented as a parallel resistance–capacitance (RC) circuit model involving a capacitor and a variable resistor. The OFF-state capacitance (C_{off}) determines the undesirable signal leakage, which is often known as 'isolation' in the OFF-state, whereas the ON-resistance (R_{on}) determines the signal loss in the ON-state, also known as the 'insertion loss.'

Traditional RF switches are made with volatile solid-state electronics such as positive–intrinsic–negative (PIN) diodes[8] or field-effect transistors (FETs)[9–11] such as III–V metal–oxide–semiconductors[19,20], III–nitride metal–oxide–semiconductors[21–23], high-electron-mobility transistors[23–25], silicon-on-insulator transistors[26,27], silicon-on-sapphire transistors[28–30], SiGe-based transistors[31–34] and bipolar complementary metal–oxide–semiconductors (BiCMOS)[32,35]. Furthermore, volatile switches based on materials such as graphene, carbon nanotubes and two-dimensional (2D) transition metal dichalcogenides (TMDs) have received a lot of attention owing to their high switching speeds, low power consumption, scalability and compatibility with existing CMOS technology[36–55]. Volatile switches consume dynamic energy during switching events as well as static energy from the standby direct current (DC) bias in the ON and OFF states. Vanadium dioxide (VO_2), a thermochromic material, also exhibits volatile switching with insulator–metal transition (IMT) at a critical temperature. Therefore, VO_2 switches have high static power consumption because they must be kept above the threshold temperature (68 °C) to maintain the conducting state[17,56,57]. RF switches based on micro-electromechanical systems (MEMS) have been investigated as a possible approach to reduce the leakage current[13,58]. However, MEMS devices are challenging to integrate with silicon CMOS technology because they are complicated and costly to manufacture and package, and they have high switching voltages (10–100 V)[12–14,59–70].

Non-volatile memory-based RF switches have zero static energy consumption; therefore, they have been intensively explored as a possible approach to develop devices with high energy efficiency, and high-frequency operations, which is particularly important for mobile systems. RF switches based on emerging non-volatile memory technologies, such as resistive random-access memory (ReRAM), conductive-bridge RAM (CBRAM), phase-change memory (PCM) and 2D memristors have been proposed. These proposed switches achieve a high cutoff frequency, small footprint, and fast and low-energy switching, and they are compatible with the standard CMOS back-end-of-line process[14–18,71–79] (Fig. 2a–d).

In this Review, we introduce emerging non-volatile RF switch technologies and compare them with mature transistor switches. We discuss the properties and mechanisms of non-volatile resistive switching (NVRS) devices based on 2D materials. Then, comprehensive RF switches based on monolayer 2D materials are described in detail, including device fabrication, high-frequency performance, switching time, power handling, and electromagnetic and thermal simulations. We also highlight the potential applications of 2D RF switches in data communication systems. Finally, we outline current challenges and future research directions including Si CMOS integration, switched filter banks, and switched antennas for phased arrays in the development of RF circuits based on monolayer 2D materials and front-end modules for the next generation of communication systems and ubiquitous mobile applications.

Non-2D non-volatile RF switches

Non-volatile memory devices such as ReRAM, CBRAM and PCM have attracted attention as emerging RF switching components for future mobile and wireless communications. The non-volatility of these devices leads to RF switches with zero static energy consumption during the idle period, thus improving the energy efficiency, which is particularly important for mobile systems. The insertion loss of 2D RF switches decreases as frequency increases, which is close to the ideal dispersionless characteristic, unlike traditional dispersive RF switches, in which the insertion loss increases with frequency owing to parasitic inductive effects[14,18,73,76,78] (Fig. 2e). The parallel-plate ON-state capacitance (C_{on}) of 2D RF switches is parallel to the quasi-static R_{on} of the nanoscale metal–insulator–metal (MIM) device, which reduces the insertion loss. RF switches based on bulk materials have a large device size, and therefore the capacitance is negligible compared with the inductance. The detailed characteristics of emerging non-volatile RF switching technologies such as ReRAM, CBRAM and PCM are discussed below, as well as the structure, performance and recent advances of each RF switch. Comparisons of their performance with those of conventional transistors and diodes and MEMS switches are also shown (Supplementary Table 1).

ReRAM-based RF switches

ReRAM is a type of non-volatile resistive memory device fabricated as a MIM sandwiched structure that consists of an amorphous transition metal oxide layer such as titanium oxide (TiO_x)[80], hafnium oxide (HfO_x)[81], aluminium oxide (Al_xO_y)[82] and tantalum oxide (Ta_xO_y)[83] between two metal electrodes (Fig. 2a). The resistive switching mechanism
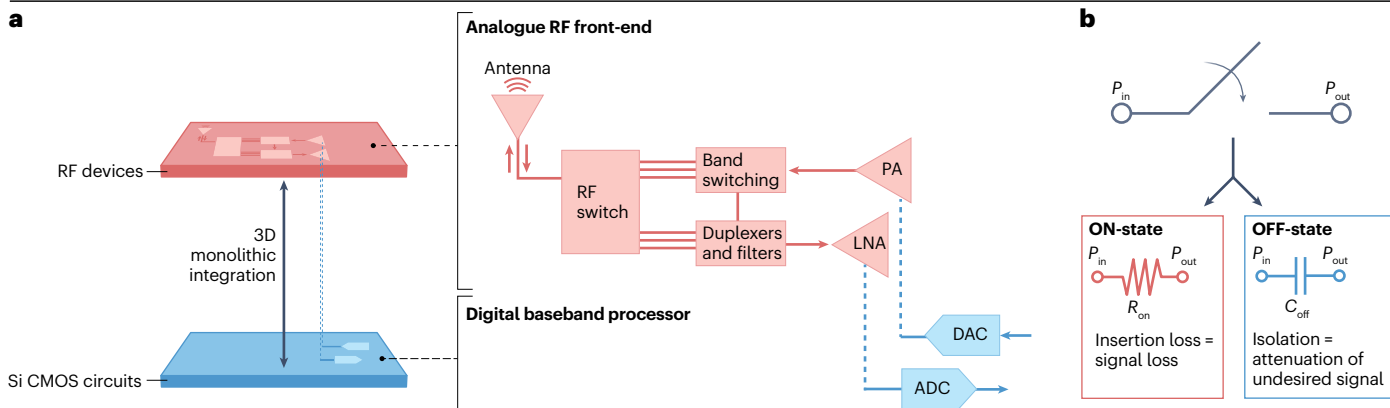
Review article

Fig. 1 | A 3D integrated radiofrequency (RF) front end and a lumped model of RF switches. a, A schematic illustration of a typical wireless radiofrequency (RF) front-end in a 3D monolithic integration structure. The upper RF devices layer transmits and amplifies the RF analogue signals, while the lower silicon complementary metal–oxide–semiconductor (Si CMOS) circuits layer converts and processes the signals. In the RF devices layer, the low-noise amplifier (LNA) amplifies the received signal, reducing noise, while the power amplifier (PA) increases the power of the transmitted signal. In the Si CMOS layer, the digital-to-analogue converter (DAC) and analogue-to-digital converter (ADC) convert the digital and analogue signals for wireless communication and baseband processing, respectively. **b**, The most basic RF switch model with ON-state resistance R_{on}, and OFF-state capacitance C_{off}. R_{on} determines insertion loss, which is the signal attenuation caused by impedance, while C_{off} determines isolation, which is the switch's effectiveness in blocking the signal. P_{in} and P_{out} indicate the input and output RF power, respectively.

of ReRAM is based on the intrinsic formation and recombination of oxygen vacancies across the amorphous oxide material. Therefore, a high electroforming (or soft breakdown) voltage of about 1.2–3.5 V is required to generate a conductive path composed of oxygen vacancies and initiate switching between the high-resistance state (HRS) and low-resistance state (LRS). These devices have been studied as energy-efficient memory and neuromorphic computing components owing to the low ON/OFF-state current of less than 100 nA and fast switching speed of a few tens of nanoseconds[82,84].

However, there are challenges associated with using ReRAM devices as RF switching components, owing to the high electroforming voltage and ON-state resistance. The oxide-based RF switch was initially built with a 30-nm-thick TiO_{2-x} active layer and platinum (Pt) metal electrodes[85]. The mesa-structured switch was fabricated as a coplanar waveguide (CPW) and achieved 10-GHz RF switching. The insertion loss and isolation at 10 GHz were 2.1 dB and 32 dB, respectively; therefore, the minimum ON-state resistance and maximum OFF-state resistance were estimated to be 28 Ω and 35 kΩ, respectively. Because of the thick (30-nm) oxide layer, the ON-state resistance is high, but the OFF-state capacitance is small (~2.5 fF). It is generally difficult to deposit uniform, pinhole-free and defect-free metal oxide films with nanometre thickness using RF sputtering and atomic layer deposition; therefore, these devices often have high leakage currents and low stability. The endurance of ReRAM-based RF switches is limited to tens of cycles, but this can be improved through material and structural optimization, such as optimizing oxide sputtering conditions, studying the metal electrodes, and varying device active area sizes[85]. Through these approaches, several TaO_x-based ReRAMs have been developed with endurances of over 10^{11} cycles[86,87].

CBRAM-based RF switches

CBRAM is an electrochemical metallization memory device that has the same MIM structure as ReRAM and consists of an air gap or insulator between two electrochemically asymmetric metal electrodes (Fig. 2b).

The electrochemically active metal electrodes, such as Ag, Cu and Ni, require a diffusion barrier to prevent oxidation and contamination in conventional CMOS technologies. Diffusion barriers, such as TiN or TaN, are thin films that are inserted between two other materials to prevent them from interdiffusing. The inert metal electrodes are usually based on metals such as W, Pt and Au, among which, W is the most commonly used one because of its prevalence in the CMOS interconnect. An applied electric field is used to induce the formation of a metallic filament from the active metal electrodes to the inert metal to set the device to the LRS. The application of an electric field in the opposite direction can rupture the filament through joule heating to return to the HRS. CBRAM-based devices have high ON/OFF ratios, low switching voltages, fast switching speeds and long retention times[88].

The resistance of these devices strongly depends on current compliance, the maximum current that can be delivered by a current source[89]. The ON-state resistance can be reduced by increasing the current compliance, acting as an optimal RF switch to minimize the insertion loss. The SET and RESET voltages are the voltages required to switch the device from its LRS to its HRS and vice versa, respectively. A laterally structured CBRAM-based RF switch on a silicon dioxide (SiO_2)-covered high-resistivity silicon (HRSi) substrate with a 35-nm-thick air gap and asymmetric Ag/Au metal electrodes demonstrated SET and RESET voltages of 3.0 V and −0.4 V, with an ON/OFF ratio of around 10^{12} (ref. 18). The insertion loss and isolation of this switch were 0.33 dB and 30 dB, respectively, at 40 GHz, and the ON-state resistance and OFF-state capacitance were 3.6 Ω and 1.4 fF, respectively, with a calculated cutoff frequency ($F_{CO} = 1/2\pi R_{on}C_{off}$) of 35 THz. Despite advantageous switching performances, the instability of the filament and risk of electrode oxidation present severe reliability issues, which can lead to high device-to-device and cycle-to-cycle variations. Generally, the design of CBRAM devices involves a tradeoff between ON-resistance and OFF-capacitance. Reducing the gap between the metal plates can shorten the filament length, resulting in lower ON-resistance. However, a smaller gap also increases the
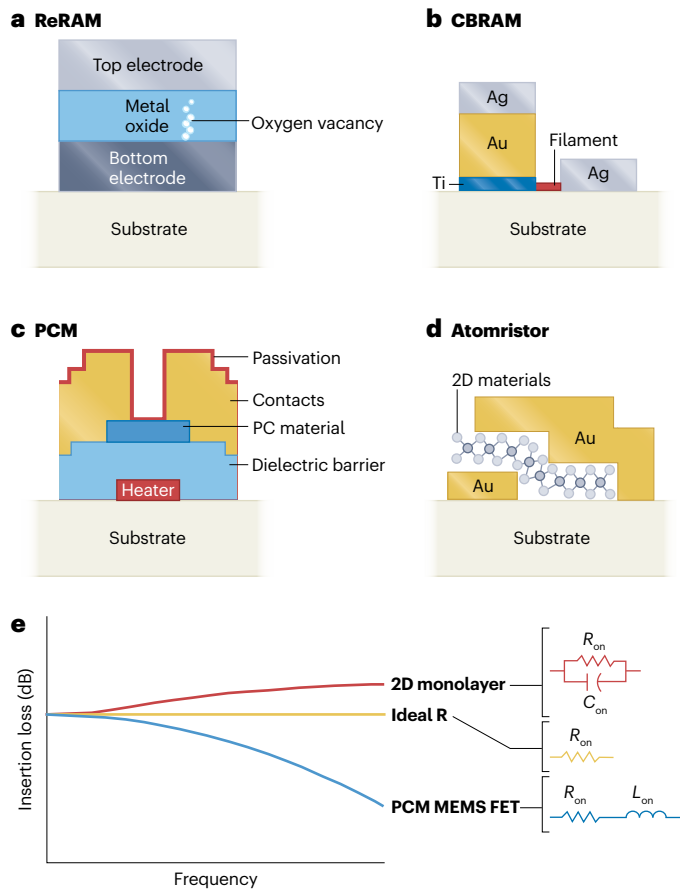
Review article

Fig. 2 | Illustration and performance comparison of various radiofrequency switch technologies. a, Resistive random-access memory (ReRAM)-based switches in which oxygen vacancies form a conductive path in the transition metal oxide layer located between two metal electrodes. **b**, In a conductive-bridge RAM (CBRAM)-based switch, metal ions migrate into the insulating material, forming a conductive filament. **c**, Inline phase-change memory (PCM) switches can be programmed by changing the phase of the phase-change (PC) material between crystalline and amorphous states. **d**, RF switches based on 2D materials have a vertical metal–insulator–metal structure, consisting of two metal electrodes separated by a thin layer of 2D materials. **e**, The characteristic insertion loss profile for a 2D atomic switch (red), an ideal resistor (R, yellow), and PCMs, micro-electromechanical systems (MEMS) and field-effect transistors (FETs) (blue). The insets show circuit diagrams for the three types of systems. R_{on}, ON-state resistance; C_{on}, ON-state capacitance; L_{on}, ON-state inductance. Part **e** reproduced with permission from ref. 135, IEEE.

and crystalline phases, spanning four orders of magnitude[91]. The reversible phase transition between the amorphous phase (HRS) and the crystalline phase (LRS) can be thermally activated through electrical actuation pulses. To make the phase-change material amorphous, a fast-speed high-amplitude RESET pulse is applied to raise the temperature above its melting temperature (T_{melt}). It is then quickly cooled and does not recrystallize anymore. A moderate-amplitude long-pulse-width SET pulse is used to crystallize the material with a pulse-induced temperature between the crystallization temperature (T_{crys}) and T_{melt}. The resistance state can be read with a small-amplitude READ pulse, which must not elevate the temperature of the device above T_{crys} (Fig. 3a).

PCM RF switches with two, three and four terminals have been proposed as promising candidates for next-generation RF switching components. The HRS/LRS ratio varies from 10^4 to 10^6 depending on the combination of chalcogenide compounds used[92–94]. Germanium telluride (GeTe)[95–98] and antimony telluride (Sb_2Te_3)[93] have relatively low ON-state resistance compared with other chalcogenide compounds, making them the top candidates for RF switches. Although two-terminal devices are heated directly, three- and four-terminal devices can be heated either directly or indirectly. In directly heated switches, the joule heating current flows through the phase-change materials whereas in indirectly heated switches the signal route is isolated from the actuation route (Fig. 2c). Hence, indirectly heated four-terminal PCM switches are useful for achieving independent actuation and RF paths, similar to transistor-based RF switches. However, indirectly heated devices are inherently less efficient than directly heated devices because the heat needs to propagate from the heater to the PCM through a dielectric layer. Hence, the device geometry must be optimized to maximize the thermal efficiency together with the RF performance[99].

A two-terminal GeTe-based RF switch was shown to have an excellent insertion loss of less than 0.20 dB and isolation of around 30 dB up to the X-band[100]. In this device, the ON-state resistance and OFF-state capacitance of 0.07 Ω mm and 20 fF mm^{-1}, respectively, enable a cutoff frequency of 80 THz. Moreover, the switch shows the highest power handling capacity of 3 W for the shunt and 10 W for the series configuration among the PCM-based switching devices with harmonic power suppression of more than 100 dBc (Fig. 3b). Additionally, more than 1 billion cycling endurance was demonstrated for a chalcogenide-based phase-change material four-terminal switch with cutoff frequency values of around 25 THz (ref. 75).

The maturity of this technology and the vast material processing knowledge of the semiconductor industry allowed the PCM RF switches to become the first industry-ready resistive-memory-based RF switch[75,101]. PCM RF switches are already applied to CMOS and SiGe BiCMOS processes with endurance and retention of more than 10^9 cycles and 10 years, respectively[35,102]. Furthermore, power handling larger than 35 dBm can be achieved, enabling the application of these devices in tunable inductors, redundant switch matrix and true-time delay phase shifters[78,103–106]. Nonetheless, PCM-based RF switches have intrinsic limitations on switching speed and energy efficiency owing to the slow crystallization time of the PCM, the large heat capacitance of the inline phase-change switch structure, lateral heat spreading, trade-offs between heat conductivity of the layers, and heat sink losses to the substrate[107]. Once the inherent limitations of endurance for reconfigurable systems and monolithic integration with standard processes are improved, PCM RF switches are likely to transition from prototype laboratories to industry-level manufacturing facilities.

OFF-state capacitance because the distance between the metal plates is reduced. Therefore, another design strategy, such as reducing the overlap area of the metal electrode, is required to reduce OFF-state capacitance. This approach also has obstacles, for instance the finite scalability of the top electrode due to fabrication limitations such as the resolution of lithography and lift-off processes.

PCM-based RF switches

PCM is a family of non-volatile memories based on chalcogenide compounds of the ternary germanium antimony telluride ($Ge_xSb_yTe_z$)[90]. These materials have a high resistance ratio between the amorphous

Review article

Two-dimensional non-volatile resistive memory

NVRS, that is, the ability to switch between a HRS and a LRS and retain the switched state even when the power supply is removed, has been observed in various 2D materials, such as graphene oxides, black phosphorus, TMDs and hexagonal boron nitrides (hBN)[77,108–117]. Large leakage currents are an issue in the nanoscale scaling in metal-oxide-based memory devices with vertical MIM architectures. However, 2D materials can overcome the vertical scaling barrier of typical MIM structure NVRS devices. Unlike amorphous metal oxide materials, 2D TMD and hBN monolayers can shrink the vertical MIM structures to nanoscale levels and realize non-volatile switching memory without excess leakage current owing to their stable crystalline structures and bandgaps that limit leakage currents. In memristive devices based on 2D materials, known as atomristors, the switching occurs in an atomically thin nanomaterial. Such devices outperform memristors based on other 2D material multilayer structures owing to their forming-free characteristic, low switching voltage, large ON/OFF ratio, atomically thin switching layer and fast switching speed. However, atomristors exhibit low endurance (10^1–10^2 cycles)[77,117,118] with respect to the multilayer 2D material based memristors (10^4–10^8 cycles)[76,119–121].

NVRS in 2D monolayers

2D monolayers are atomically thin sheets of materials that have unique properties, such as high electrical conductivity, mechanical strength, and flexibility. These properties make 2D monolayers ideal candidates for developing next-generation electronic devices, including NVRS memory devices. The NVRS mechanism in an $Au/MoS_2/Au$ device comprising a monolayer MoS_2 in a MIM structure is driven by the adsorption and desorption of Au atoms into intrinsic sulfur vacancy sites[77,122]

(Fig. 4a,b). When a forward voltage is applied from 0 to 1.2 V under 10-mA current compliance, the Au atoms dissociate from the Au electrode and absorb into the sulfur vacancy sites to form conductive points between the MoS_2 monolayer and Au electrode, switching from HRS to LRS. When the forward voltage is swept back to 0 V, the Au atoms remain bound at the vacancy sites, indicating that the device remains in LRS. Conversely, when the reverse bias is applied from 0 to −1.5 V without current compliance, the Au atoms desorb from the vacancy sites and return to the electrode, returning the device to a HRS. When the reverse voltage is swept from −1.5 to 0 V, the device remains in the HRS[77,122,123].

The variance in switching characteristics between devices could be caused by multiple factors, including material qualities, manufacturing methods, and structural variations. Notably, atomristors exhibit an electroforming-free feature, in which the NVRS operation starts with a soft dielectric breakdown to generate a conductive filament, which is essential for metal-oxide memristors. The metal-oxide electroforming process can be avoided by decreasing the thickness to the few-nanometre regime; however, the decreased thickness often results in trap-assisted tunnelling with a high leakage current. Atomristors produce sharp interfaces and clean tunnel barriers, demonstrating their superiority over thin amorphous metal oxides by achieving an ON/OFF ratio greater than 10^4 (ref. 124). Such properties are not exclusive to MoS_2; similar resistive switching results have been observed in other monolayer TMDs (WS_2, ReS_2, $MoSe_2$, WSe_2, $ReSe_2$) and hBN. These results suggest that NVRS is a universal phenomenon in non-metallic 2D monolayers[122].

In addition to DC operation, pulse measurements can be used to apply a voltage at nanosecond timescales to avoid overheating or overstressing the device under test (Fig. 4c). In the case of a monolayer
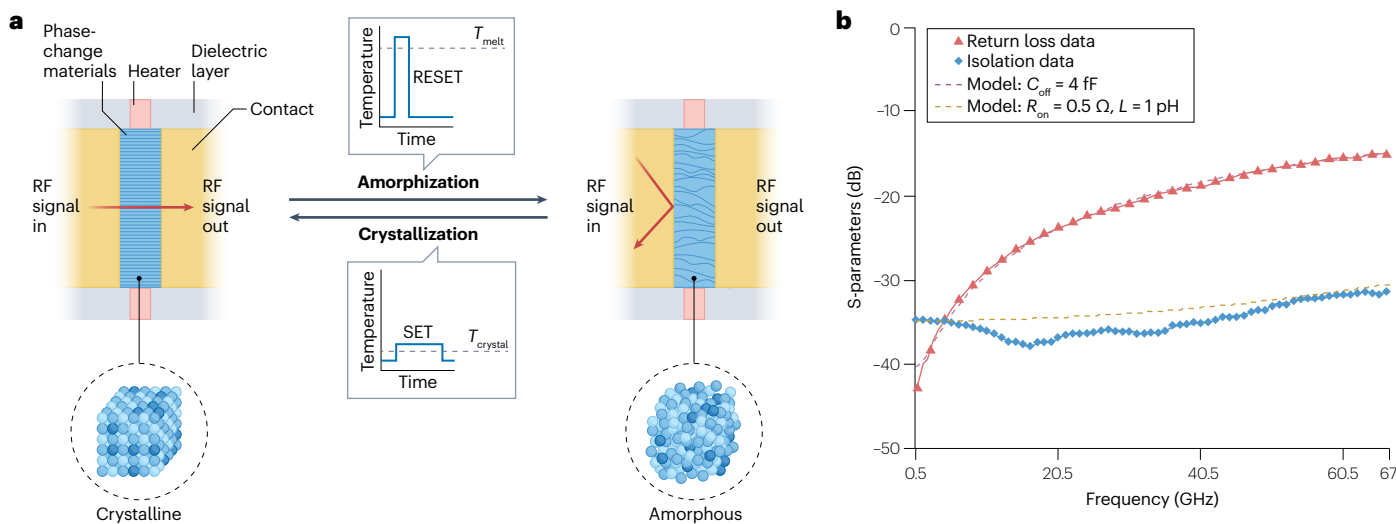

Fig. 3 | Structures and characteristics of phase-change-memory-based radiofrequency switches. a, To set phase-change memory (PCM) cells, a high temperature above the amorphization temperature is applied for a short duration (RESET, top). To return the PCM cells to a crystalline phase, a low temperature above the crystallization temperature is applied for a long duration (SET, bottom). In the crystalline phase (left), PCM transmits a radiofrequency (RF) signal, whereas in the amorphous phase (right), it stops the RF signal. The left and right insets illustrate a typical crystalline structure and an amorphous structure of phase-change material, respectively. **b**, Measured (red triangles and blue diamonds) and modelled (dashed line) return loss and isolation of GeTe

PCM shunt RF switches. S-parameters are a set of scattering parameters that describe the electrical behaviour of linear electrical networks at their ports. Return loss is a measure of how much of the incident power at a port is reflected back, and isolation is a measure of how much coupling there is between two ports of a network. A high return loss indicates that the circuit is well matched to the transmission line, and a high isolation indicates that there is very little coupling between the two ports. These parameters are important for minimizing signal losses and improving the performance of RF and microwave circuits. Part **b** reproduced with permission from ref. 100, IEEE.
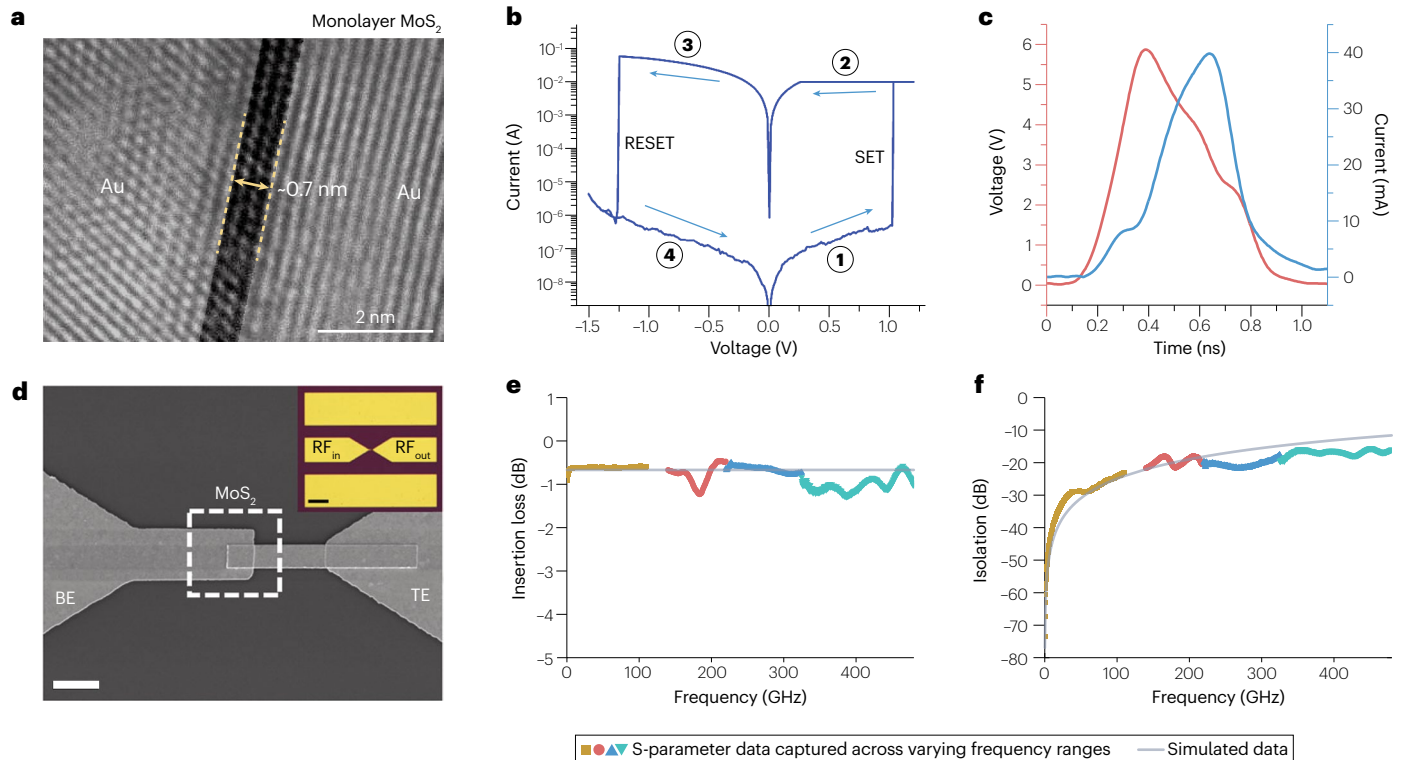
Review article

Fig. 4 | Structures and characteristics of 2D radiofrequency switches.
a, A transmission electron microscopy cross-section image of the atomically sharp and clear monolayer interface of $Au/MoS_2/Au$. **b**, Representative measured current–voltage curve of bipolar resistive switching behaviour in a $2 \times 2\ \mu m^2$ lateral area monolayer MoS_2 crossbar device. Step 1: Switch the device from the high-resistance state (HRS) to the low-resistance state (LRS) by applying a voltage from 0 to 1.2 V. The current will increase to the compliance current (10 mA). Step 2: Maintain the device in the LRS. Sweep the voltage from 1.0 V to 0 V. Step 3: Reset the device from the LRS to the HRS by sweeping the voltage from 0 V to -1.5 V. Step 4: Maintain the device in the HRS. Sweep the voltage from −1.5 V to 0 V. **c**, Applying a 500-ps, 5-V SET pulse to a monolayer MoS_2 memristor measures the voltage (red) and current (blue) through the device as it switches from the OFF to the ON state. **d**, A scanning electron microscopy image of a MoS_2 radiofrequency (RF) switch. The dashed box indicates the vertical metal–insulator–metal structure with an overlap area of $0.5 \times 0.5\ \mu m^2$. The inset shows an optical image of a ground–signal–ground coplanar waveguide layout. BE and TE represent bottom electrode and top electrode, respectively. RF_{in} and RF_{out} are the input and output ports of an RF circuit, respectively. **e,f**, Scattering parameter (S-parameter) measured and modelled in both the (**e**) ON (insertion loss) and (**f**) OFF (isolation) states of an RF switch based on a $0.15 \times 0.2\ \mu m^2$ monolayer MoS_2 atomristor. Insertion loss is a measure of how much the signal is attenuated as it passes through a component; isolation is a measure of how much coupling there is between two ports of a network. Different colours indicate the different measurement frequency ranges: 0.25–110.00 GHz (yellow), 140–220 GHz (red), 220–325 GHz (blue) and 325–480 GHz (cyan). The grey lines show the S-parameters of the extracted equivalent lumped element circuit model. Parts **a** and **b** reproduced with permission from ref. 77, American Chemical Society. Parts **c**, **e** and **f** reproduced from ref. 127, Springer Nature. Part **d** reproduced from ref. 76, Springer Nature.

MoS_2 memristor, the equivalent switching energy of 50 pJ is orders of magnitude lower than that of modern PCM RF switches[5,7].

Two-dimensional RF switches

High-performance analogue and RF switches have gained interest as fundamental components in reconfigurable radio systems[6]. An ideal RF switch consumes zero static power and a finite amount of dynamic power during switching. Non-volatile switches based on ReRAM, CBRAM, PCM and 2D memristors have been developed to create energy-efficient switches[5,14,73,76,125,126]. For these memory devices to be used as RF switches, they should have low ON-state resistance ($R_{on} < 10\ \Omega$), and low OFF-state capacitance ($C_{off} < 10$ fF) to attain a high cutoff frequency in the THz range. Monolayer MoS_2 films were used to fabricate 2D RF switches that operate at up to 480 GHz with an experimental data rate of 100 Gbit/s which corresponds to

IEEE 6G data communication standards. Additionally, hBN switches with an experimental data rate of 8.5 Gbit/s for 5G bands have been demonstrated[127,128]. In terms of energy consumption, switching speed and operating voltages, these analogue switches based on 2D material outperform other emerging RF switches such as ReRAM and PCM (Supplementary Table 1).

Device fabrication and structure

Similar to other non-volatile RF switch technologies such as ReRAM, CBRAM and PCM, 2D RF switches also have a vertical MIM structure and consist of two metal electrodes with a 2D material in between (Fig. 2d). RF switches based on 2D materials can be fabricated on a 300-μm-thick chemical vapour deposited diamond substrate with a root-mean-square surface roughness of less than 0.8 nm (ref. 76). Diamond substrates are preferred to silicon or SiO_2/Si substrates because they have a high

Review article

thermal conductivity, which enables heat to dissipate, preventing overheating on the metal feedlines during DC and RF measurements for reliable operation[129]. Electron beam lithography followed by 2-nm Cr/150-nm Au metal deposition has been used to pattern the top and bottom electrodes on a diamond substrate. The 2D atomic layers can then be placed on the bottom electrode using either the poly(methyl methacrylate)-assisted wet transfer method or the poly-dimethylsiloxane stamp transfer method[117,130–132]. Using the described fabrication process, an MoS$_2$ RF switch was made with a ground–signal–ground CPW design and a device overlap area of 0.5×0.5 μm^2 in a vertical MIM structure[76] (Fig. 4d).

High-frequency performance of 2D RF switches

The high-frequency S-parameters, a set of parameters that characterize the performance of RF and microwave devices, can be measured using a vector network analyser. On-wafer calibrations are needed to remove the extrinsic influences of the measurement wiring and probe stations, and therefore to obtain precise results. Intrinsic S-parameters of RF switches can then be acquired using de-embedding methods to remove probe–pad and interconnect resistances on the same substrate[133]. A monolayer MoS$_2$ switch was shown to exhibit a small insertion loss in the ON-state (Fig. 4e) and isolation below 15 dB in the OFF-state at frequencies up to 480 GHz (Fig. 4f). Three performance parameters, R_{on}, C_{off} and F_{CO}, can be calculated with an equivalent lumped element circuit model[18,70]. After de-embedding the S-parameters to remove the effects of the test fixture, the intrinsic R_{on} and C_{off} values were extracted from the de-embedded S-parameters in the ON and OFF states. The MoS$_2$ RF switches were found to exhibit higher cutoff frequencies (70 THz) than other emerging RF switch technologies such as solid-state, MEMS and PCM switches.

MIMO, reliability and scaling of 2D RF switches

To achieve multiple-input and multiple-output (MIMO) circuit applications in ubiquitous systems operating at RF and 5G frequencies, MoS$_2$-based single-pole–double-throw (SPDT) switches have been developed[134]. In the DC-50 GHz bandwidth, SPDT switches achieved insertion losses below 2 dB and isolation over 10 dB with a compliance current of 10 mA and overlap device areas of 1×1 μm^2 at high frequencies. The extracted R_{on} and C_{off} values for two switches are 13.5 Ω, 20 Ω and 6.5 fF, 6 fF, respectively, indicating that they can be used to implement a MIMO system[134] (Fig. 5a). To achieve practical applications with stability, retention performance should be considered, as the device must maintain its states without volatility. S-parameter measurements show that typical 2D RF switches exhibit stable ON and OFF states over 3 months at room temperature in air[126] (Fig. 5b).

In traditional solid-state, PCM and MEMS RF switches, the area scaling limits insertion loss for isolation because C_{off} increases while R_{on} decreases with the increasing overlap area. However, the isolation of RF switches based on 2D materials can be increased without increasing loss, because R_{on} is area-independent and C_{off} is proportional to the overlap area[76]. For 2D RF switches, electromagnetic simulation results of the correlation of C_{off} to the MIM overlap area (Fig. 5c) exhibit an anticipated parallel-plate capacitance dependency in large overlap areas and an unexpected saturation (~1 fF) for smaller overlap areas, which limits the design parameters[135]. C_{off} saturation can be explained using the CPW structure, in which the overlap area can be precisely adjusted through lithography, while the parasitic capacitance remains constant for a given C_{off}.

In addition, it is crucial to address the thermal heat generation in high-power RF devices. A finite element analysis (FEA) simulation can provide the temperature distribution in the heated area of RF switches built on SiO$_2$/Si, Si and diamond substrates and the dependence of output powers on input RF signal powers[126] (Fig. 5d). Diamond has a higher thermal conductivity than SiO$_2$/Si and Si substrates and thus could be used as a potential heat sink. The surface-area average temperatures obtained using electrothermal simulations are comparable to those obtained in thermal measurements, which suggests electrothermal simulations could be a useful tool for thermal management in the system[126] (Fig. 5e). High switch reliability is critical for high-signal-power applications such as transmitters, since high signal power can induce signal distortion and losses. Therefore, the simulation platforms can help examine or optimize a variety of device topologies and emerging RF switches for thermal management.

Power handling and linearity performance

The highest power a switch can transmit in the ON-state while maintaining excellent isolation in the OFF-state is referred to as RF power handling. In the ON-state, the output power of both MoS$_2$ and hBN RF switches increases linearly with input RF signal power, with little signal losses[126]. Because atomristors have a low actuation voltage, RF power-induced adjustable self-switching is an attractive application for a tunable attenuator. In the OFF state, the output power exhibits large losses and a linear relationship with input power before rapidly losing isolation owing to self-bias from the high-power RF signal, which causes 'self-switching' from the OFF to the ON state. Self-switching in hBN RF switches occurs at 20 dBm, which is close to the DC switching voltage when feedline losses are considered[126].

Intermodulation distortion is an important metric for evaluating the nonlinearity of high-frequency devices. High RF input power can cause self-heating in devices, affecting their electrical properties, resulting in nonlinearity owing to fluctuations in the ON-state resistance. A vector network analyser is used to generate and inject the two input tones (f_1 = 2.365 GHz and f_2 = 2.415 GHz) with a power sweep from −30 to +10 dBm. The basic signal and third-order intermodulation product show slopes of 1 and 3, respectively, indicating that MoS$_2$ RF switches exhibit good linearity[126,135] (Fig. 5f).

Applications of non-volatile RF switch technology

Non-volatile RF switch technology is an emerging technology that has the potential to advance a wide range of applications, from mobile communication systems to satellite communication systems to radar systems. Non-volatile RF switches are able to retain their state even after power is removed, making them ideal for applications where reconfigurability and low power consumption are important considerations.

RF switches for 6G data communications

The rapid advances in connectivity systems and wireless communication leads to an urgent need to increase data rates to meet the ever-growing demand. Edholm's bandwidth law postulates that the bandwidth of telecommunications networks doubles every 18 months[136]. Since the early 2000s, wireless data traffic has grown at an exponential rate, and it is predicted that wireless data rates will be able to compete with wired internet by 2030 (refs. 4,137) (Fig. 6a). RF switches are essential components for 6G data communication. Additionally, they can address the demanding connectivity requirements of augmented reality (AR) and virtual reality (VR) applications by enabling ultrahigh data rates, low latency, massive device connectivity, beam-forming and MIMO, high energy efficiency, millimetre-wave
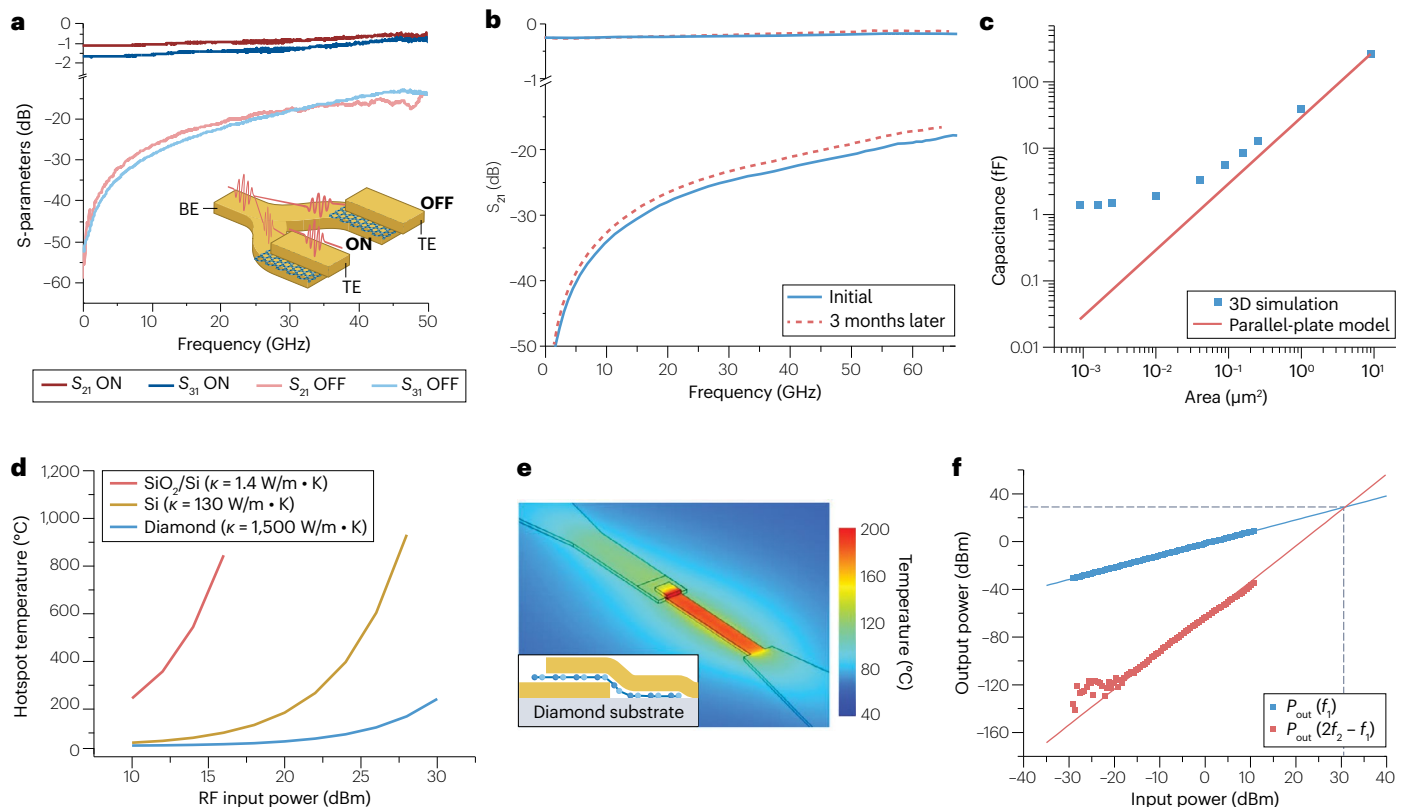
Fig. 5 | Multiple-input and multiple-output, retention, scaling and thermal properties of 2D radiofrequency switches. a, S-parameters are a set of scattering parameters that describe the electrical behaviour of linear electrical networks at their ports. De-embedded S_{21} and S_{31} represent the S-parameters of a single-pole–double-throw (SPDT) $1 \times 1\,\mu m^2$ switch from port 1 to ports 2 and 3, respectively. The inset illustration shows that the SPDT device effectively blocks the signal for the OFF-state port and transmits it through the ON-state port. The measured S-parameters confirm that the device can be used for a multiple-input and multiple-output (MIMO) system. BE and TE denote the bottom electrode and top electrode, respectively. **b**, Comparing the initial S-parameter of hexagonal boron nitride (hBN) monolayer-based RF switch (blue line) with the S-parameter measured 3 months later (red dashed line) confirms the stability of the device. The upper two lines indicate the insertion loss in the ON-state, and the lower two lines indicate the isolation in the OFF-state. **c**, The OFF-state capacitances of the parallel-plate model (red line) of RF switch agree well with the results of the 3D electromagnetic simulation (blue squares) for large overlap areas. However, for small areas, parasitic and edge capacitances begin to dominate, resulting in a scale-invariant capacitance. **d**, The simulated hotspot temperature of an RF switch on a 300-nm SiO_2/bulk Si (red curve), bulk Si (yellow curve) or diamond (blue curve) substrate. This simulation shows that diamond substrates have better heat sinking capabilities than SiO_2/Si and bulk Si, owing to diamond's high thermal conductivity, κ. **e**, A simulation of the temperature of hBN RF switch at an input RF power of 29.3 dBm, showing that a high-temperature hotspot occurs near the vertical metal–insulator–metal (MIM) structure. The inset shows a side view of the hBN monolayer-based RF switch. **f**, Intermodulation distortion (IMD) is a type of distortion that occurs when two or more signals are mixed together, causing interference and reduced signal quality. IMD measurement was conducted to assess the linearity of a monolayer MoS_2 RF switch in the ON-state ($f_1 = 2.365$ GHz; $f_2 = 2.415$ GHz; $2f_2 - f_1 = 2.465$ GHz). f_1 and f_2 are the fundamental frequencies of the two input signals. $2f_2 - f_1$ is the third-order intermodulation product (IM3) frequency. Based on the two fundamental frequencies (f_1 and f_2) with the same input RF power, the output power signal contains the fundamental, $P_{out}(f_1)$, and third-harmonic ($2f_2 - f_1$) frequencies, $P_{out}(2f_2 - f_1)$. The red and blue solid lines are visual guidelines for IMD extrapolation. The cross-section point represents the input intercept (IIP3) and output intercept (OIP3) points. The ON-state IMD graph of the fundamental frequency (f_1) and third-order intermodulation ($2f_2 - f_1$) signal shows 31 dBm third-order IIP3 and 30 dBm third-order OIP3. Part **a** reproduced with permission from ref. 134, IEEE. Parts **b**, **d** and **e** reproduced from ref. 126, copyright 2020, Springer Nature. Part **c** reproduced with permission from ref. 135, IEEE. Part **f** reproduced from ref. 127, Springer Nature.

communication, seamless handovers and edge computing integration. These capabilities will make AR and VR experiences more immersive, interactive and responsive[1–3].

Baud rate is the unit of measurement for the symbol rate of a digital signal, which is the number of symbols transmitted per second. High baud rate, high spectral efficiency and sophisticated modulations are necessary for high-bandwidth data transmission and reception performance. The functionality of the MoS_2 switch has been verified with various modulation schemes, amplitude phase-shift keying with 16 symbols (APSK16); quadrature phase-shift keying (QPSK) for 10 and 25 GBaud (20 and 50 Gbit/s, respectively); and quadrature amplitude modulation (QAM) with 16, 32 and 64 symbols (QAM16, QAM32 and QAM64, respectively). The evolution of signal-to-noise ratio (SNR) for various modulation schemes and data rates shows that more complex modulation schemes can be used to achieve higher data rates at a given SNR (Fig. 6b). The data rate for QAM16 achieved 100 Gbit/s, which
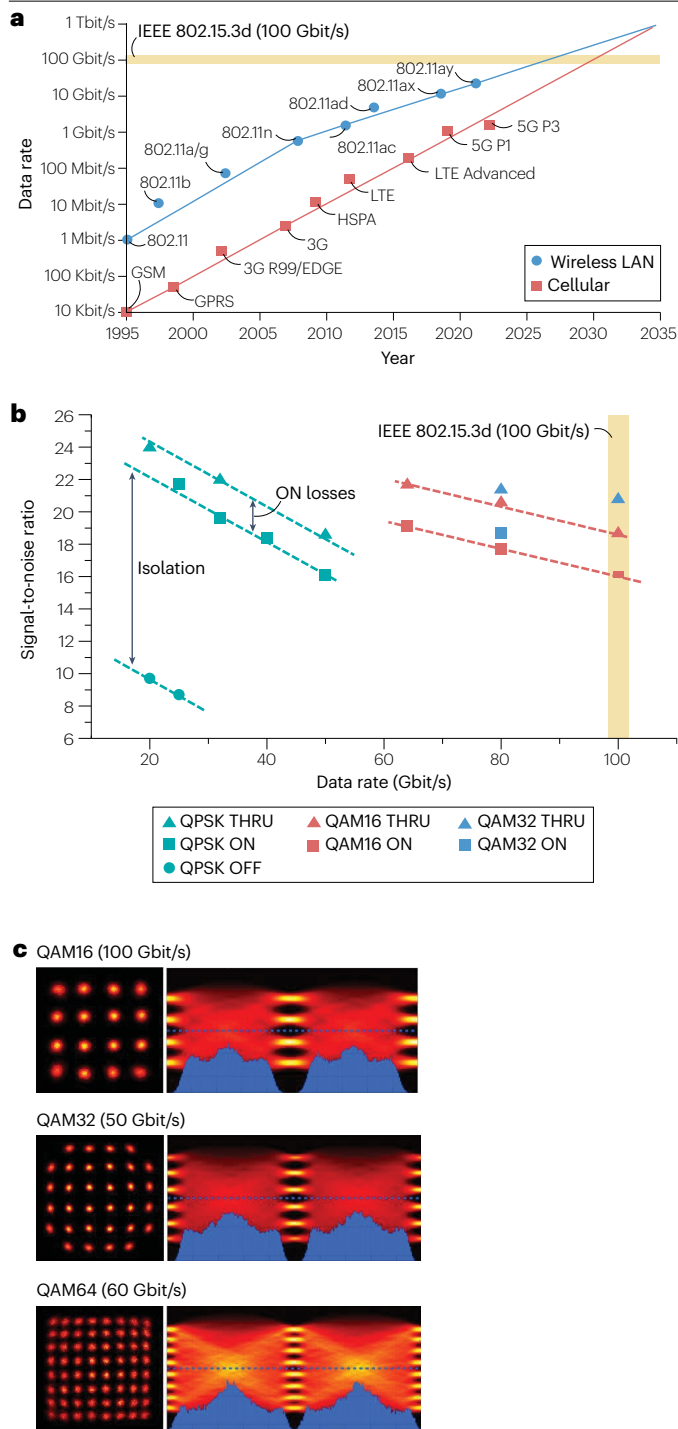
Review article

Fig. 6 | Data communication properties of 2D radiofrequency switches.
a, Outlook for the data rate of wireless local area networks (LANs) and cellular networks. The yellow band at 100 Gbit/s complies with IEEE 802.15.3d, the IEEE 6G standard for high-data-rate wireless multimedia networks. Wireless LAN communication standards (IEEE 802.11, 802.11b, 802.11a/g, 802.11n, 802.11ad, 802.11ax, and 802.11ay) and cellular communication standards (GSM, GPRS, 3G R99/EDGE, 3G, HSPA, LTE, LTE Advanced, 5G P1, 5G P3) define the frequency bands, modulation schemes and data rates for these communication systems. Each subsequent generation of standards typically offers improved data rate, capacity, and spectral efficiency over the previous one. **b**, The signal-to-noise ratio (SNR) versus data rate plot shows how much data can be transmitted over a channel with a given SNR. These plots are important for designing and optimizing data communication systems. The measured SNR of monolayer MoS_2 RF switches showing good signal quality for various data rates and modulation schemes. Data rate is the speed at which data is transmitted over a communication channel. Modulation scheme is the method used to encode digital data onto a physical signal. The data rate target of the 6G standard (IEEE 802.15.3d) is indicated by the yellow band at 100 Gbit/s. THRU, ON and OFF represent measurements of the metal line, the ON-state and the OFF-state of the MoS_2 RF switch, respectively. Quadrature phase-shift keying (QPSK) is a digital modulation scheme that uses four phase shifts to represent two bits of data per symbol. Quadrature amplitude modulation (QAM) is a digital modulation scheme that uses both amplitude and phase modulation to represent data. QAM is more efficient than QPSK, but it is also more complex and more susceptible to noise. The green and red dashed lines are visual guides that connect QPSK and QAM16 points, respectively, showing a decreasing SNR trend with increasing data rate. **c**, A constellation diagram is a graphical representation of a modulated signal, showing its amplitude and phase at different symbol times. An eye diagram is a graphical representation of a modulated signal synchronized to the symbol clock, showing its timing jitter and amplitude distortion. Both constellation diagrams and eye diagrams can be used to diagnose problems with a communication system, evaluate its performance and design new communication systems. Left, representative constellation diagrams for MoS_2 devices with 100, 50 and 60 Gbit/s data rates with QAM16, QAM32 and QAM64 modulation methods at ON-state. Right, the corresponding eye diagrams with the blue spectra indicating the eye-crossing section. Both constellation diagrams and eye diagrams demonstrate that successful data modulation is achieved on 2D RF switches. Part **b** reproduced from ref. 127, Springer Nature. Part **c** reproduced with permission from ref. 128, IEEE.

meets the aim of the IEEE 802.15.3d release for 6G networks operating in the 300 GHz range. Constellation diagrams and eye diagrams of MoS_2 devices show negligible distortions under various modulation schemes, indicating high-quality signal transmission (Fig. 6c). The MoS_2 switch handled high-level QAM64 modulation, which is a proposed modulation technique in the IEEE 802.15.3d standard for future THz communication. Following the high-data-rate characterizations with in-phase/quadrature (I/Q) modulations, real-time high-data-rate video streaming was investigated to ensure that the switch can handle real-time data streams encoded in the THz bands for 6G applications[127].

RF switches for RF front-end systems

With the rising use of mobile devices, demand is growing for a wireless communication ecosystem to support a broader range of RF standards, including 5G, 6G and satellite communications. To this end, cognitive radio systems have been explored as a potential solution. These systems constantly sense the idle frequency ranges, and then dynamically reconfigure the transceiver to operate in the white spaces of the frequency spectrum. In such systems, isolation between circuit components is important because the operation must be unaffected by other components, as signal interference can corrupt the desired signal, increase bit error rate or cause interruptions in service. High-performance RF switches are key components for reconfigurable radio systems that enable customized RF functions for numerous frequency bands as well as the coexistence of multiple wireless communication standards (Fig. 7a). Thus, with such architectures, blocks can be reused and unnecessary components removed, enabling increased flexibility while substantially decreasing system costs, development time, form factor and wireless front-end complexity. High-performance RF switches
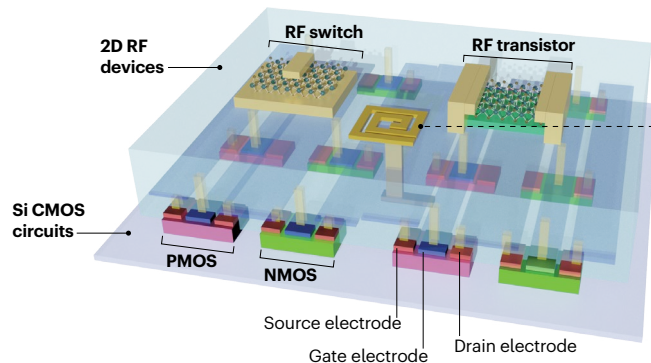
Review article

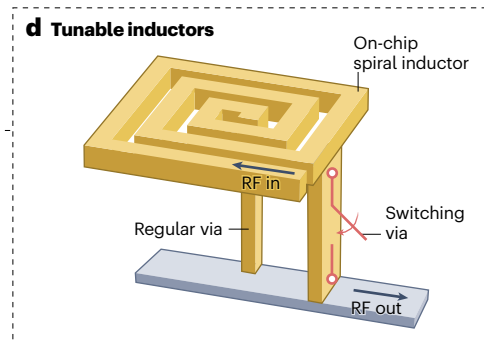**a** Cognitive RF systems
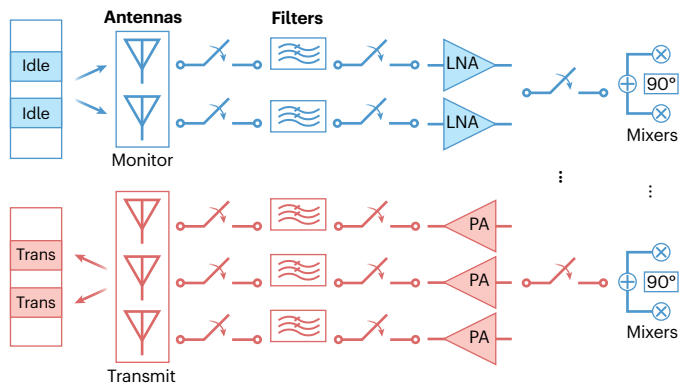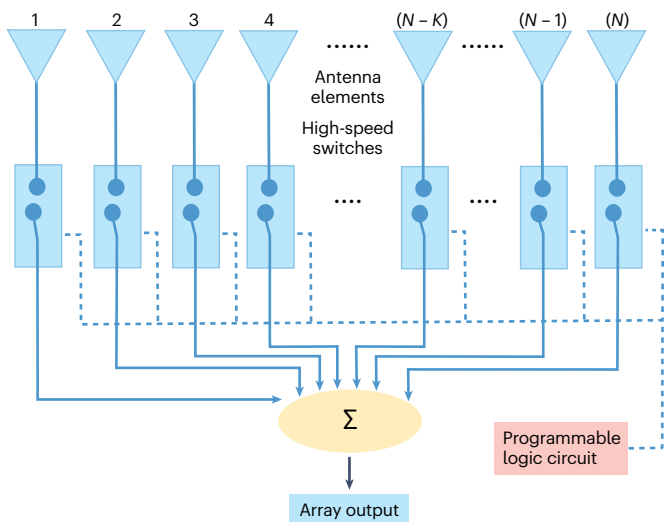
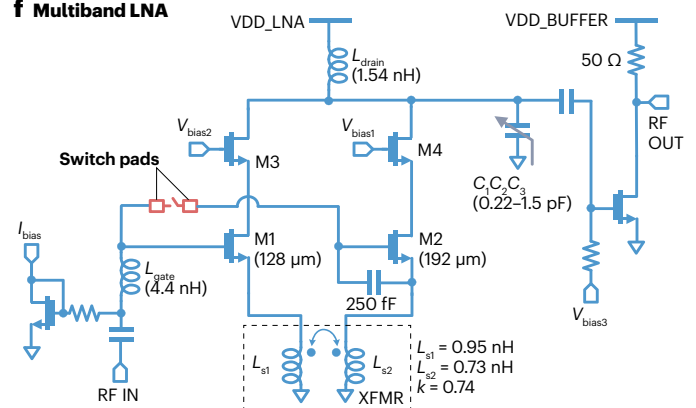**b** Switched filter bank
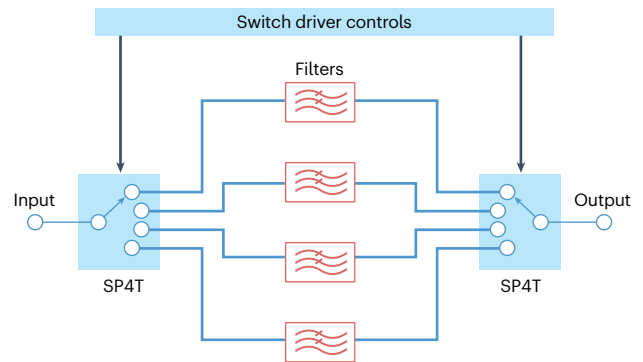
c 3D-MMIC

d Tunable inductors

e Switched antenna

f Multiband LNA

based on resistive switching devices could be used in applications such as tunable inductors, capacitors, filters, attenuators, antennas, phase shifters, switched oscillators and amplifiers (Fig. 7).

To exploit this possibility, RF switches that are compatible with standard CMOS processes with a small footprint, good transmission performance, low power consumption, and low actuation voltage are required. 2D RF switches can be readily fabricated on any

substrate; therefore, they can be integrated with Si CMOS technology using three-dimensional monolithic microwave integrated circuit (3D-MMIC) structures or through-silicon vias to increase functionality density[138–141]. Placing RF and logic devices on the same layer can make them susceptible to coupling noise, a type of electrical noise that can interfere with the desired signal and degrade the performance of the system. Separated layer integration can overcome this problem and

Review article

a, High-performance radiofrequency (RF) switches can be used to reconfigure the connection between various front-end blocks in cognitive radio systems. As shown in the top blue figures, the antennas monitor the idle band, and the filter is selected by switching, depending on the operating frequency. The signal is amplified by a low-noise amplifier (LNA) to reduce received signal noise. Then, the mixers change the received frequency so that the signal can be processed by the baseband processor. Conversely, the bottom red figures show that the power amplifier (PA) amplifies the magnitude of the transmitting signal, allowing it to reach a greater distance. The filter is selected by switching to transmit the signal in the idle band. **b**, A switched filter bank is a device that uses switches to select between multiple filters, allowing a single device to perform multiple filtering operations. The block diagram shows a switched filter bank with single-pole–four-throw (SP4T) switches. **c**, Three-dimensional monolithic microwave integrated circuits (3D-MMICs) can be heterogeneously integrated with vertical interconnects, enabling the monolithic integration of emerging RF components, such as 2D RF switches, transistors, and inductors, onto complementary metal–oxide–semiconductor (CMOS) logic baseband processors, which are composed of *p*-channel metal–oxide–semiconductor (PMOS) and *n*-channel metal–oxide–semiconductor (NMOS) transistors. **d**, The structure of a tunable spiral inductor consists of a regular via and a tunable conductive-bridge random-access memory (CBRAM) via. The regular via is always connected to the RF input signal. When the switching via is turned off, the signal flows through the regular via, resulting in a longer total length and more turns. On the other hand, when the switching via is turned on, the signal flows through it, resulting in a shorter total length and fewer turns. **e**, Phased-array antenna architecture with high-speed switches and programmable logic circuits can enable beam steering by changing the phase of the antenna. The desired phase can be controlled by adjusting the phase shift of each antenna element. N and K are arbitrary integers that depend on the desired antenna system. **f**, Schematic of a dual-band LNA using phase-change memory (PCM) RF switches. This single LNA can resonate at both 3 GHz and 5 GHz. When the PCM switch is ON, the LNA operates at 3 GHz due to the parallel capacitance of the first and second cascode stages. When the PCM switch is OFF, the LNA operates at 5 GHz as the second cascode stage is removed. RF IN and RF OUT denote the RF input and output signals, respectively. M1, M2, M3 and M4 represent transistors that constitute two cascode legs. I_{bias}, V_{bias1}, V_{bias2} and V_{bias3} denote the supplied direct current and voltage for RF biasing. VDD_LNA and VDD_BUFFER denote the supplied voltage for LNA and buffer operation, respectively. k denotes the coupling factor of the XFMR (transformer). L_{s1} and L_{s2} represent inductors used to implement the high-k XFMR. C_1, C_2 and C_3 are capacitors in the inductor–capacitor tank load, which enable band selection. L_{gate} and L_{drain} represent inductors for conjugate matching, connected to the gate and drain, respectively. Part **e** reproduced from ref. 145, Springer Nature. Part **f** reproduced with permission from ref. 147, IEEE.

increase design flexibility and power efficiency[24,142]. Furthermore, reducing the length of the interconnects between layers reduces the parasitic effects of capacitance and inductance and the possibility of signal loss or interference, as well as reducing electromagnetic interference issues because there are fewer current loops[142]. These more-than-Moore 3D-MMIC devices could combine logic, memory, sensors, antennas, analogue and RF circuits from several front-end manufacturing modules into a single system using heterogeneous integration (Fig. 7c).

Tunable inductors. Tunable inductors are versatile components that offer more flexibility and control in circuit design and can be used to implement a wider range of circuit functions. They are used in a variety of applications, including RF filters, tunable oscillators and impedance matching circuits. A wire loop and a cross layer are used in RF inductors to give access to the second electrode; therefore, 2D memristor-based RF switches could be placed between the two layers to change the effective length of inductors. This approach was verified with a circuit simulation that demonstrated that a CBRAM switch can function as a switching channel to change the number of loops N of an inductor, hence changing its inductance[143] (Fig. 7d).

Switched filter banks. RF filters are electronic devices that pass signals within a certain frequency range and attenuate signals outside that range, and are used in a wide variety of applications, including communication systems, radar systems, and test and measurement equipment. A switched filter bank is made up of single-pole multiple-throw (SPNT) input and output RF switches, as well as a set of filters for each channel (Fig. 7b). By integrating a filter and a switching matrix in a single module, circuit transitions are eliminated, allowing for better matching with improved insertion loss, flatness, voltage standing wave ratio and overall performance. Using a switched filter bank in an MMIC based on 2D materials instead of multiple filters can decrease the weight, cost and overall size of filter systems, making them suitable for use in mobile phones, drones, aeroplanes and satellites.

Switched antenna for phased arrays. High-frequency signals are highly directional but vulnerable to noise. The MIMO approach has been developed to overcome this limitation, by using fixed arrays of phased antennas to control the direction of each signal by adjusting the time delays and phase differences. A key antenna selection technique involves sequentially turning on and off antennas in a large array to transmit signals with precise time delays.

To fabricate phased-array antenna systems with both switched-beam and beam-steering characteristics, 2D RF switches can be integrated in analogue phase shifters and switched-line to adjust the phase delay angles between the array antennas[144,145] (Fig. 7e). The beam-forming capability of this system can be used to produce a highly directed radiation pattern in the direction of a mobile device, improving the channel capacity and receiver SNR.

Multiband low-noise amplifiers. LNAs are crucial to improving the overall performance of adaptive systems because they are the first active stage after the antenna in a radio transceiver. LNAs are made up of many switchable amplifying transistors, capacitors and/or inductors to achieve a low noise figure (NF), high gain and good input matching over a wide range of frequency bands[146].

A dual-band LNA has been demonstrated with a four-terminal indirectly heated PCM RF switch with 0.13-m CMOS technology[147]. The LNA is composed of two common sources that have source degeneration and are switched by a PCM RF switch (Fig. 7f). For 3 and 5 GHz, the LNA exhibits low NF (2.85 and 2.86 dB) and high gain (19.5 and 20 dB). However, when the switch is used over a single LNA, the gain is reduced by less than 2 dB and the NF is reduced by 1 dB. This shows that the RF switch can tune the LNA very well to meet the application needs.

Programmable voltage-controlled oscillator. A tunable voltage-controlled oscillator (VCO) is essential for an RF front-end because it allows for a wide range of carrier frequencies, which is critical for RF front-ends that operate in multiple frequency bands. It is used as a local oscillator in frequency synthesizers to generate

Review article

modulated signals using local carriers, which influences the overall performance of the radio. The key design challenges are tuning the oscillation frequency range, phase noise and output power level[148–150].

An inductor–capacitor (LC) cross-coupled VCO can be built using tunable inductors based on non-volatile resistive RF switches. Using 0.13-m CMOS technology and a PCM RF switch-based switchable inductor, VCOs were developed in two modes: series-connected (SC) and coupled-controlled (CC)[151]. The SC topology uses a PCM RF switch to bypass a part of the inductor, allowing the VCO to detect a change in inductance. In contrast, the CC topology makes use of a two-winding inductor. The SC (CC) topology achieves broad tuning ranges for OFF/ON-states of 2.89–4.23 (4.93–7.79) GHz and 4.80–8.53 (5.28–10.20) GHz.

Conclusions and outlook

Although substantial advances in the development of 2D RF switches have been made, several challenges must be addressed to advance the design of more efficient switches. First, the endurance of 2D RF switches should be increased to ensure stable device functioning in practical communication and connectivity systems. Second, RF switches must handle higher power levels for 6G, radar and connectivity systems, while being compatible with other high-power components without causing distortion or noise. Integrated power amplifiers and high-power immune RF switches are a suitable solution for cutting-edge practical RF front-end systems by providing wider bands and band combinations while enhancing power efficiency and chip density. However, contemporary 2D RF switches only have linearity up to 0.1 W, which is 100 times smaller than the linearity range of conventional volatile PIN- and FET-based switches. Finally, 2D material synthesis methods need further progress in wafer-scale reproducibility and uniformity, coupled with transfer integration in the back-end-of-the-line of industrial semiconductor technology for circuit design and chip realization. Alternatively, the direct growth of 2D materials on industrial chip wafers might also be effective, but, for this purpose, it is important to ensure a low synthesis temperature compatible with back-end-of-the-line processes.

Next-generation wireless communication based on 6G technologies will require low latency, high bandwidth, high THz operating frequencies (carrier frequencies around 300 GHz) and complex modulation techniques. As these technologies continue to evolve, the seamless integration of 6G connectivity and RF switching technologies will be crucial for realizing their full potential in gaming, entertainment, education, commerce, training and beyond. As a result, switches need further improvement to satisfy 6G frequency and data-rate criteria with zero static power dissipation. RF switches based on 2D materials can enable the expansion of their applications for future wireless communication and connection systems spanning from mobile to aerospace, automotive, medical, infrastructure, AR and VR.

References

1. Lu, Y. & Zheng, X. 6G: a survey on technologies, scenarios, challenges, and the related issues. *J. Ind. Inf. Integr.* **19**, 100158 (2020).
2. Saad, W., Bennis, M. & Chen, M. A vision of 6G wireless systems: applications, trends, technologies, and open research problems. *IEEE Netw.* **34**, 134–142 (2019).
3. Siriwardhana, Y., Porambage, P., Liyanage, M. & Ylianttila, M. A survey on mobile augmented reality with 5G mobile edge computing: architectures, applications, and technical aspects. *IEEE Commun. Surv. Tutor.* **23**, 1160–1192 (2021).
4. Elayan, H., Amin, O., Shihada, B., Shubair, R. M. & Alouini, M.-S. Terahertz band: the last piece of RF spectrum puzzle for communication systems. *IEEE Open. J. Commun. Soc.* **1**, 1–32 (2019).

5. Wainstein, N., Adam, G., Yalon, E. & Kvatinsky, S. Radiofrequency switches based on emerging resistive memory technologies — a survey. *Proc. IEEE* **109**, 77–95 (2020).
   This review offers a fundamental understanding of radiofrequency (RF) switch technologies based on resistive memory.
6. Olsson, R. H., Bunch, K. & Gordon, C. Reconfigurable electronics for adaptive RF systems. In *2016 IEEE Compound Semiconductor Integrated Circuit Symposium (CSICS)*, https://doi.org/10.1109/CSICS.2016.7751061 (IEEE, 2016).
7. Yalon, E. et al. Energy-efficient indirectly heated phase change RF switch. *IEEE Electron. Device Lett.* **40**, 455–458 (2019).
8. Lee, J.-L., Zych, D., Reese, E. & Drury, D. M. Monolithic 2–18 GHz low loss, on-chip biased PIN diode switches. *IEEE Trans. Microw. Theory Tech.* **43**, 250–256 (1995).
9. Larson, L. E. Integrated circuit technology options for RFICs — present status and future directions. *IEEE J. Solid-State Circuits* **33**, 387–399 (1998).
10. Li, Q., Zhang, Y. P., Yeo, K. S. & Lim, W. M. 16.6- and 28-GHz fully integrated CMOS RF switches with improved body floating. *IEEE Trans. Microw. Theory Tech.* **56**, 339–345 (2008).
11. Syroiezhin, S., Oezdamar, O., Weigel, R. & Solomko, V. Switching time acceleration for high-voltage CMOS RF switch. In *IEEE 48th European Solid State Circuits Conference (ESSCIRC)*, 301–304 (IEEE, 2022).
12. Brown, E. R. RF-MEMS switches for reconfigurable integrated circuits. *IEEE Trans. Microw. theory Tech.* **46**, 1868–1880 (1998).
13. Stefanini, R., Chatras, M., Blondy, P. & Rebeiz, G. M. Miniature MEMS switches for RF applications. *J. Microelectromech. Syst.* **20**, 1324–1335 (2011).
14. Patel, C. D. & Rebeiz, G. M. A compact RF MEMS metal-contact switch and switching networks. *IEEE Microw. Wirel. Compon. Lett.* **22**, 642–644 (2012).
15. Wang, M. & Rais-Zadeh, M. Development and evaluation of germanium telluride phase change material based ohmic switches for RF applications. *J. Micromech. Microeng.* **27**, 013001 (2017).
16. El-Hinnawy, N. et al. Origin and optimization of RF power handling limitations in inline phase-change switches. *IEEE Trans. Electron. Devices* **64**, 3934–3942 (2017).
17. Madan, H. et al. 26.5 Terahertz electrically triggered RF switch on epitaxial VO₂-on-sapphire (VOS) wafer. In *2015 IEEE International Electron Devices Meeting (IEDM)*, 9.3.1–9.3.4 (IEEE, 2015).
   This article describes a wafer-scale epitaxial VO₂ on sapphire insulator–metal transition RF switch with a 26.5-THz cutoff frequency.
18. Pi, S., Ghadiri-Sadrabadi, M., Bardin, J. C. & Xia, Q. Nanoscale memristive radiofrequency switches. *Nat. Commun.* **6**, 7519 (2015).
   This article presents a nanoscale air-gap conductive bridge RF switch that has a low programming voltage, a high ON/OFF ratio and long retention time.
19. Bijesh, R. et al. Demonstration of In₀.₉Ga₀.₁As/GaAs₀.₁₈Sb₀.₈₂ near broken-gap tunnel FET with I_ON=740 µA/µm, G_M=70 µS/µm and gigahertz switching performance at V_DS=0.5 V. In *2013 IEEE International Electron Devices Meeting (IEDM)*, 28.22.21–28.22.24 https://doi.org/10.1109/IEDM.2013.6724708 (IEEE, 2013).
20. Ali, A. et al. Enhancement-mode antimonide quantum-well MOSFETs with high electron mobility and gigahertz small-signal switching performance. *IEEE electron. device Lett.* **32**, 1689–1691 (2011).
21. Moon, J.-S. et al. High-speed linear GaN technology with a record efficiency in Ka-band. In *2019 14th European Microwave Integrated Circuits Conference (EuMIC)*. 57–59 (IEEE, 2019).
22. Simin, G. et al. High-power RF switching using III-nitride metal-oxide-semiconductor heterojunction capacitors. *IEEE electron. device Lett.* **26**, 56–58 (2005).
23. Fletcher, A. A. & Nirmal, D. A survey of gallium nitride HEMT for RF and high power applications. *Superlattices Microstruct.* **109**, 519–537 (2017).
24. Jeong, J. et al. In *2021 Symposium on VLSI Technology*, 1–2 (IEEE, 2021).
25. Yore, M. D., Nevers, C. A. & Cortese, P. High-isolation low-loss SP7T pHEMT switch suitable for antenna switch modules. In *5th European Microwave Integrated Circuits Conference*, 69–72 (IEEE, 2010).
26. Wang, D. et al. High performance SOI RF switches for wireless applications. In *10th IEEE International Conference on Solid-State and Integrated Circuit Technology*, 611–614 (IEEE, 2010).
27. Tinella, C., Fournier, J.-M., Belot, D. & Knopik, V. A high-performance CMOS-SOI antenna switch for the 2.5-5-GHz band. *IEEE J. Solid-State Circuits* **38**, 1279–1283 (2003).
28. Kelly, D. J. CMOS-on-sapphire RF switches for cellular handset applications. In *Proc. Conf. CS MANTECH, April 14–17, 2008* (Citeseer, 2008).
29. Kelly, D., Brindle, C., Kemerling, C. & Stuber, M. The state-of-the-art of silicon-on-sapphire CMOS RF switches. In *IEEE Compound Semiconductor Integrated Circuit Symposium CSIC'05*, https://doi.org/10.1109/CSICS.2005.1531812 (IEEE, 2005).
30. Novak, R. in *2013 International Symposium on VLSI Design, Automation, and Test (VLSI-DAT)*, 1 (IEEE, 2013).
31. Shi, Y., Ren, J., Deng, Y., Fay, P. & Liu, L. High-performance optically controlled rf switches for advanced reconfigurable millimeter-wave-to-THz circuits. In *2019 IEEE MTT-S International Microwave Conference on Hardware and Systems for 5G and Beyond (IMC-5G)*. https://doi.org/10.1109/IMC-5G47857.2019.9160365 (IEEE, 2019).
32. Madan, A., Cressler, J. & Joseph, A. A high-linearity inverse-mode SiGe BiCMOS RF switch. In *2010 IEEE Bipolar/BiCMOS Circuits and Technology Meeting (BCTM)*, 61–64 (IEEE, 2010).
33. Cheon, C. D. et al. A new wideband, low insertion loss, high linearity SiGe RF switch. *IEEE Microw. Wirel. Compon. Lett.* **30**, 985–988 (2020).

Review article

34. Hancock, T. M. & Rebeiz, G. M. Design and analysis of a 70-ps SiGe differential RF switch. *IEEE Trans. Microw. Theory Tech.* **53**, 2403–2410 (2005).
35. Slovin, G., El-Hinnawy, N., Masse, C., Rose, J. & Howard, D. Monolithic integration of phase-change RF switches in a production SiGe BiCMOS process with RF circuit demonstrations. In *2020 IEEE/MTT-S International Microwave Symposium (IMS)*, 57–60 (IEEE, 2020).
36. Zhu, W. et al. Black phosphorus flexible thin film transistors at gighertz frequencies. *Nano Lett.* **16**, 2301–2306 (2016).
37. Wang, J. et al. Transferred metal gate to 2D semiconductors for sub-1V operation and near ideal subthreshold slope. *Sci. Adv.* **7**, eabf8744 (2021).
38. Badmaev, A., Che, Y., Li, Z., Wang, C. & Zhou, C. Self-aligned fabrication of graphene RF transistors with T-shaped gate. *ACS Nano* **6**, 3371–3376 (2012).
39. Yeh, C.-H. et al. Gigahertz field-effect transistors with CMOS-compatible transfer-free graphene. *ACS Appl. Mater. Interfaces* **11**, 6336–6343 (2019).
40. Ivanov, T. G. et al. Diamond RF transistor technology with $f_t = 41$ GHz and $f_{max} = 44$ GHz. In *2018 IEEE/MTT-S International Microwave Symposium-IMS*, 1461–1463 (IEEE, 2018).
41. Cheng, R. et al. Few-layer molybdenum disulfide transistors and circuits for high-speed flexible electronics. *Nat. Commun.* **5**, 5143 (2014).
42. Yu, C. et al. Improvement of the frequency characteristics of graphene field-effect transistors on SiC substrate. *IEEE Electron. Device Lett.* **38**, 1339–1342 (2017).
43. Tian, M. et al. Wafer scale mapping and statistical analysis of radio frequency characteristics in highly uniform CVD graphene transistors. *Adv. Electron. Mater.* **5**, 1800711 (2019).
44. Krasnozhon, D., Lembke, D., Nyffeler, C., Leblebici, Y. & Kis, A. MoS2 transistors operating at gigahertz frequencies. *Nano Lett.* **14**, 5905–5911 (2014).
45. Gao, Q. et al. Scalable high performance radio frequency electronics based on large domain bilayer MoS₂. *Nat. Commun.* **9**, 4778 (2018).
46. Zhou, J. et al. Carbon nanotube based radio frequency transistors for K-band amplifiers. *ACS Appl. Mater. Interfaces* **13**, 37475–37482 (2021).
47. Zhou, J. et al. Carbon nanotube radiofrequency transistors with f_T/f_{MAX} of 376/318 GHz. *IEEE Electron. Device Lett.* **44**, 329–332 (2022).
48. Zhong, D. et al. Carbon nanotube film-based radio frequency transistors with maximum oscillation frequency above 100 GHz. *ACS Appl. Mater. Interfaces* **11**, 42496–42503 (2019).
49. Rutherglen, C. et al. Wafer-scalable, aligned carbon nanotube transistors operating at frequencies of over 100 GHz. *Nat. Electron.* **2**, 530–539 (2019).
50. Cao, Y. et al. Radio frequency transistors using aligned semiconducting carbon nanotubes with current-gain cutoff frequency and maximum oscillation frequency simultaneously greater than 70 GHz. *ACS Nano* **10**, 6782–6790 (2016).
51. Shi, H. et al. Radiofrequency transistors based on aligned carbon nanotube arrays. *Nat. Electron.* **4**, 405–415 (2021).
52. Zhong, D. et al. Gigahertz integrated circuits based on carbon nanotube films. *Nat. Electron.* **1**, 40–45 (2018).
53. Lin, Y.-M. et al. 100-GHz transistors from wafer-scale epitaxial graphene. *Science* **327**, 662–662 (2010).
54. Wu, Y. et al. High-frequency, scaled graphene transistors on diamond-like carbon. *Nature* **472**, 74–78 (2011).
55. Wang, H. et al. Black phosphorus radio-frequency transistors. *Nano Lett.* **14**, 6424–6429 (2014).
56. Pan, K., Wang, W., Shin, E., Freeman, K. & Subramanyam, G. Vanadium oxide thin-film variable resistor-based RF switches. *IEEE Trans. Electron. Devices* **62**, 2959–2965 (2015).
57. Anagnostou, D. E., Torres, D., Teeslink, T. S. & Sepulveda, N. Vanadium dioxide for reconfigurable antennas and microwave devices: enabling RF reconfigurability through smart materials. *IEEE Antennas Propag. Mag.* **62**, 58–73 (2020).
58. Li, M., Zhao, J., You, Z. & Zhao, G. Design and fabrication of a low insertion loss capacitive RF MEMS switch with novel micro-structures for actuation. *Solid-State Electron.* **127**, 32–37 (2017).
59. Rebeiz, G. M., Patel, C. D., Han, S. K., Ko, C.-H. & Ho, K. M. The search for a reliable MEMS switch. *IEEE Microw. Mag.* **14**, 57–67 (2013).
60. Peng, Z. et al. In *2009 IEEE MTT-S International Microwave Symposium Digest*, 1637–1640 (IEEE, 2009).
61. Majumder, S., Lampen, J., Morrison, R. & Maciel, J. A packaged, high-lifetime ohmic MEMS RF switch. In *IEEE MTT-S International Microwave Symposium Digest*, 1935–1938 (IEEE, 2003).
62. Newman, H. S., Ebel, J. L., Judy, D. & Maciel, J. Lifetime measurements on a high-reliability RF-MEMS contact switch. *IEEE Microw. Wirel. Compon. Lett.* **18**, 100–102 (2008).
63. Patel, C. D. & Rebeiz, G. M. A high power (>5 W) temperature stable RF MEMS metal-contact switch with orthogonal anchors and force-enhancing stoppers. In *2011 IEEE MTT-S International Microwave Symposium*, https://doi.org/10.1109/MWSYM.2011.5973336 (IEEE, 2011).
    This article presents the measurement of high power handling (>5 W) in RF micro-electromechanical systems switches.
64. Patel, C. D. & Rebeiz, G. M. A high-reliability high-linearity high-power RF MEMS metal-contact switch for DC–40-GHz applications. *IEEE Trans. Microw. Theory Tech.* **60**, 3096–3112 (2012).
65. Costa, J. et al. Integrated MEMS switch technology on SOI-CMOS. In Proc. Hilton Head Workshop: A Solid-State Sensors, *Actuators and Microsystems Workshop*, 900–903 (2008).
66. Wunnicke, O. et al. Small, low-ohmic RF MEMS switches with thin-film package. In *2011 IEEE 24th International Conference on Micro Electro Mechanical Systems*, 793–796 (IEEE, 2011).
67. Joshi, V. et al. A CMOS compatible back end MEMS switch for logic functions. In *2010 IEEE International Interconnect Technology Conference* 1–3 (IEEE, 2010).
68. Malmqvist, R. et al. In *40th European Microwave Conference*, 85–88 (IEEE, 2010).
69. Barrière, F., Pothier, A., Crunteanu, A., Chatras, M. & Blondy, P. In *41st European Microwave Conference*, 1229–1232 (IEEE, 2011).
70. Liu, A.-Q. *RF MEMS Switches and Integrated Switching Circuits* Vol. 5 (Springer, 2010).
71. Wong, H. S. P. et al. Metal–oxide RRAM. *Proc. IEEE* **100**, 1951–1970 (2012).
72. Wouters, D. J., Waser, R. & Wuttig, M. Phase-change and redox-based resistive switching memories. *Proc. IEEE* **103**, 1274–1288 (2015).
73. Field, M. et al. in *Open Architecture/Open Business Model Net-Centric Systems and Defense Transformation* 947908 (International Society for Optics and Photonics, 2015).
74. Chappell, W. J., Hancock, T. M. & Olsson, R. H. in *2018 IEEE/MTT-S International Microwave Symposium-IMS*, 829–831 (IEEE, 2018).
75. El-Hinnawy, N., Slovin, G., Rose, J. & Howard, D. in *2020 IEEE/MTT-S International Microwave Symposium (IMS)*, 45–48 (IEEE, 2020).
    This paper presents a four-terminal phase-change material RF switch with high endurance capability, up to 1 billion cycles.
76. Kim, M. et al. Zero-static power radio-frequency switches based on MoS₂ atomristors. *Nat. Commun.* **9**, 2524 (2018).
    This article presents a high-performance monolayer MoS₂-based RF switch.
77. Ge, R. et al. Atomristor: nonvolatile resistance switching in atomic sheets of transition metal dichalcogenides. *Nano Lett.* **18**, 434–441 (2018).
    This article demonstrates the non-volatile resistive switching characteristics of several transition metal dichalcogenide monolayers, with subnanometre scalability and low off-current.
78. Leon, A. et al. RF power-handling performance for direct actuation of germanium telluride switches. *IEEE Trans. Microw. Theory Tech.* **68**, 60–73 (2019).
79. Singh, T., Hummel, G., Vaseem, M. & Shamim, A. Recent advancements in reconfigurable mmwave devices based on phase-change and metal insulator transition materials. *IEEE J. Microw.* **3**, 827–851 (2023).
80. Park, J. et al. TiOx-based RRAM synapse with 64-levels of conductance and symmetric conductance change by adopting a hybrid pulse scheme for neuromorphic computing. *IEEE Electron. Device Lett.* **37**, 1559–1562 (2016).
81. Wang, C. et al. Ultrafast RESET analysis of HfOx-based RRAM by sub-nanosecond pulses. *Adv. Electron. Mater.* **3**, 1700263 (2017).
82. Kim, S. & Choi, Y.-K. Resistive switching of aluminum oxide for flexible memory. *Appl. Phys. Lett.* **92**, 223508 (2008).
83. Lee, T. S. et al. Compliance current-controlled conducting filament formation in tantalum oxide-based RRAM devices with different top electrodes. *ACS Appl. Electron. Mater.* **2**, 1154–1161 (2020).
84. Wei, Z. et al. In *2008 IEEE International Electron Devices Meeting* 1–4 (IEEE, 2008).
85. Ruxandra, B. Novel metal oxide resistive switches for tunable radio frequency circuits. In *Proc. Innov. Sustainability Conf.* 41–42 (2017).
86. Kim, Y.-B. et al. In *2011 Symposium on VLSI Technology — Digest of Technical Papers*, 52–53 (IEEE, 2011).
87. Lee, M.-J. et al. A fast, high-endurance and scalable non-volatile memory device made from asymmetric Ta2O5−x/TaO2−x bilayer structures. *Nat. Mater.* **10**, 625–630 (2011).
    This article reports that asymmetric Ta₂O₅₋ₓ/TaO₂₋ₓ bilayer resistive random access memory exhibits extreme cycling endurance of over 10¹², along with 10-ns switching time.
88. Nessel, J. A. et al. In *2008 IEEE MTT-S International Microwave Symposium Digest*, 1051–1054 (IEEE, 2008).
89. Su, Y.-T. et al. Characteristics of hafnium oxide resistance random access memory with different setting compliance current. *Appl. Phys. Lett.* **103**, 163502 (2013).
90. Mennai, J. et al. In *2015 European Microwave Conference (EuMC)*, 945–947 (IEEE, 2014).
91. Wuttig, M. & Yamada, N. Phase-change materials for rewriteable data storage. *Nat. Mater.* **6**, 824–832 (2007).
92. Moon, J.-S. et al. In *2018 IEEE Radio and Wireless Symposium (RWS)*, 231–233 (IEEE, 2018).
93. Moon, J.-S. et al. Reconfigurable infrared spectral imaging with phase change materials. In *Micro- and Nanotechnology Sensors, Systems, and Applications XI* (2019).
94. Moon, J.-S. et al. In *2018 IEEE/MTT-S International Microwave Symposium-IMS*, 836–838 (SPIE, 2018).
95. Moon, J.-S., Seo, H.-C. & Le, D. In *2014 IEEE 14th Topical Meeting on Silicon Monolithic Integrated Circuits in RF Systems*, 7–9 (IEEE, 2014).
96. Moon, J.-S. et al. In *2015 IEEE MTT-S International Microwave Symposium*, 1-4 (IEEE, 2015).
97. Moon, J.-S. et al. In *2015 IEEE 15th Topical Meeting on Silicon Monolithic Integrated Circuits in RF Systems*, 73–75 (IEEE, 2015).
98. Singh, T. & Mansour, R. R. Experimental investigation of performance, reliability, and cycle endurance of nonvolatile DC–67 GHz phase-change RF switches. *IEEE Trans. Microw. Theory Tech.* **69**, 4697–4710 (2021).
99. Slovin, G. et al. Design criteria in sizing phase-change RF switches. *IEEE Trans. Microw. Theory Tech.* **65**, 4531–4540 (2017).
100. Moon, J.-S., Seo, H.-C. & Le, D. In *2014 IEEE MTT-S International Microwave Symposium (IMS2014)*, 1–3 (IEEE, 2014).
    This article discusses the high-power handling property of germanium telluride-based phase-change materials and their potential applications.
101. Slovin, G., El-Hinnawy, N., Moen, K. & Howard, D. In *2021 IEEE International Electron Devices Meeting (IEDM)*, 4.4.1–4.4.4 (IEEE, 2021).

Review article

102. Cheng, H.-Y. et al. In *2015 IEEE International Electron Devices Meeting (IEDM)*, 3.5.1–3.5.4 (IEEE, 2015).
103. Wen, C.-Y. et al. In *2010 International Electron Devices Meeting*, 10.13.11–10.13.14 (IEEE, 2010).
104. Singh, T. & Mansour, R. R. Miniaturized DC–60 GHz RF PCM GeTe-based monolithically integrated redundancy switch matrix using T-type switching unit cells. *IEEE Trans. Microw. Theory Tech.* **67**, 5181–5190 (2019).
105. Singh, T. & Mansour, R. R. In *2019 49th European Microwave Conference (EuMC)*, 180–183 (IEEE, 2019).
106. El-Hinnawy, N. et al. In *2021 IEEE MTT-S International Microwave Symposium (IMS)*, 424–427 (IEEE, 2021).
107. Wainstein, N., Ankonina, G., Kvatinsky, S. & Yalon, E. Compact modeling and electrothermal measurements of indirectly heated phase-change RF switches. *IEEE Trans. Electron. Devices* **67**, 5182–5187 (2020).
108. Qi, M. et al. Uniform multilevel switching of graphene oxide-based RRAM achieved by embedding with gold nanoparticles for image pattern recognition. *Appl. Phys. Lett.* **116**, 163503 (2020).
109. Wang, L.-H. et al. The mechanism of the asymmetric SET and RESET speed of graphene oxide based flexible resistive switching memories. *Appl. Phys. Lett.* https://doi.org/10.1063/1.3681366 (2012).
110. Wu, M. et al. Covalent functionalization of black phosphorus nanosheets with photochromic polymer for transient optoelectronic memory devices. *Adv. Electron. Mater.* **9**, 2200925 (2023).
111. Puglisi, F. M. et al. In *2016 IEEE International Electron Devices Meeting (IEDM)*, 34.38.31–34.38.34 (IEEE, 2016).
112. Zhu, K. et al. Graphene–boron nitride–graphene cross-point memristors with three stable resistive states. *ACS Appl. Mater. Interfaces* **11**, 37999–38005 (2019).
113. Villena, M. A. et al. Variability of metal/h-BN/metal memristors grown via chemical vapor deposition on different materials. *Microelectron. Reliab.* **102**, 113410 (2019).
114. Bertolazzi, S. et al. Nonvolatile memories based on graphene and related 2D materials. *Adv. Mater.* **31**, 1806663 (2019).
115. Wu, X., Ge, R., Kim, M., Akinwande, D. & Lee, J. C. In *2020 Pan Pacific Microelectronics Symposium (Pan Pacific)*, 1–6 (IEEE, 2020).
116. Ki Hong, S., Eun Kim, J., Kim, S. O. & Jin Cho, B. Analysis on switching mechanism of graphene oxide resistive memory device. *J. Appl. Phys.* **110**, 044506 (2011).
117. Wu, X. et al. Thinnest nonvolatile memory based on monolayer h-BN. *Adv. Mater.* **31**, e1806790 (2019).
118. Li, Y. et al. Resistive switching properties of monolayer h-BN atomristors with different electrodes. *Appl. Phys. Lett.* **120**, 173104 (2022).
119. Chen, S. et al. Wafer-scale integration of two-dimensional materials in high-density memristive crossbar arrays for artificial neural networks. *Nat. Electron.* **3**, 638–645 (2020).
120. Nikam, R. D., Rajput, K. G. & Hwang, H. Single-atom quantum-point contact switch using atomically thin hexagonal boron nitride. *Small* **17**, 2006760 (2021).
121. Wang, M. et al. Robust memristors based on layered two-dimensional materials. *Nat. Electron.* **1**, 130–136 (2018).
122. Ge, R. et al. A library of atomically thin 2D materials featuring the conductive-point resistive switching phenomenon. *Adv. Mater.* **33**, 2007792 (2021).
123. Hus, S. M. et al. Observation of single-defect memristor in an MoS₂ atomic sheet. *Nat. Nanotechnol.* **16**, 58–62 (2021).
      This article provides insights into the origin of the non-volatile resistive switching mechanism in atomic sheets, using monolayer MoS₂ as a model system.
124. Bhattacharjee, S. et al. Insights into multilevel resistive switching in monolayer MoS₂. *ACS Appl. Mater. Interfaces* **12**, 6022–6029 (2020).
125. Léon, A. et al. In *2018 48th European Microwave Conference (EuMC)*, 491–494 (IEEE, 2018).
126. Kim, M. et al. Analogue switches made from boron nitride monolayers for application in 5G and terahertz communication systems. *Nat. Electron.* **3**, 479–485 (2020).
      This article demonstrates the affordability of monolayer hBN RF switches for terahertz communication, with low bit error rate and power consumption.
127. Kim, M. et al. Monolayer molybdenum disulfide switches for 6G communication systems. *Nat. Electron.* **5**, https://doi.org/10.1038/s41928-022-00766-2 (2022).
      This article reports the high-frequency operation of monolayer MoS₂ switches up to 480 GHz, and demonstrates their potential for use in 6G applications by showing eye diagrams and constellation diagrams at various data rates.
128. Kim, M. et al. In *2022 IEEE/MTT-S International Microwave Symposium — IMS 2022*, 902–905 (IEEE, 2022).
129. Railkar, T. A. et al. A critical review of chemical vapor-deposited (CVD) diamond for electronic applications. *Crit. Rev. Solid. State Mater. Sci.* **25**, 163–277 (2000).
130. Lee, Y. H. et al. Synthesis and transfer of single-layer transition metal disulfides on diverse surfaces. *Nano Lett.* **13**, 1852–1857 (2013).
131. Chang, H. Y. et al. Large-area monolayer MoS₂ for flexible low-power RF nanoelectronics in the GHz regime. *Adv. Mater.* **28**, 1818–1823 (2016).
132. Yu, Y. et al. Controlled scalable synthesis of uniform, high-quality monolayer and few-layer MoS₂ films. *Sci. Rep.* **3**, 1866 (2013).
133. Cha, J., Cha, J. & Lee, S. Uncertainty analysis of two-step and three-step methods for deembedding on-wafer RF transistor measurements. *IEEE Trans. Electron. Devices* **55**, 2195–2201 (2008).
134. Kim, M., Pallecchi, E., Happy, H. & Akinwande, D. In *2021 Device Research Conference (DRC)*, 1–2 (IEEE, 2021).
135. Kim, M. et al. Non-volatile RF and mm-wave switches based on monolayer hBN. In *2019 IEEE International Electron Devices Meeting (IEDM)*, 9.5.1–9.5.4 (IEEE, 2019).
136. Cherry, S. Edholm's law of bandwidth. *IEEE Spectr.* **41**, 58–60 (2004).
137. Li, R. In *Proc. 3rd Annu. ITU IMT-2020/5G Workshop Demo Day*, 1–21.
138. Kaho, T. et al. In *2007 European Microwave Integrated Circuit Conference*, 12–15 (IEEE, 2007).
139. Kim, J.-Y., Ju, X., Ang, K.-W. & Chi, D. Van der Waals layer transfer of 2D materials for monolithic 3D electronic system integration: review and outlook. *ACS Nano* **17**, 1831–1844 (2023).
140. Liu, Y. et al. Promises and prospects of two-dimensional transistors. *Nature* **591**, 43–53 (2021).
141. Zhu, K. et al. Hybrid 2D–CMOS microchips for memristive applications. *Nature* **618**, 57–62 (2023).
142. Jeong, J. et al. Heterogeneous and monolithic 3D integration of III–V-based radio frequency devices on Si CMOS circuits. *ACS Nano* **16**, 9031–9040 (2022).
      This article demonstrates the feasibility of heterogeneous and monolithic 3D analogue and RF-digital mixed-signal integrated circuits with no performance degradation.
143. Wainstein, N. & Kvatinsky, S. TIME — tunable inductors using memristors. *IEEE Trans. Circuits Syst. I Regul. Pap.* **65**, 1505–1515 (2017).
      This article reports the simulation of a tunable inductor application based on memristors, using both the memristive-via and the multilayer stacked inductor topologies.
144. Tsai, Y.-C., Chen, Y.-B. & Hwang, R.-B. Combining the switched-beam and beam-steering capabilities in a 2-D phased array antenna system. *Radio. Sci.* **51**, 47–58 (2016).
      This paper presents the development, fabrication and measurement of a beam-forming antenna array system.
145. Chakraborty, A., Ram, G. & Mandal, D. Classification of attacks on MQTT-based IoT system using machine learning techniques. In *International Conference on Innovative Computing and Communications: Proc. ICICC 2021* Vol. 3, 205–216 (Springer, 2021).
146. Razavi, B. Architectures and circuits for RF CMOS receivers. In *Proc. IEEE 1998 Custom Integrated Circuits Conference*, 393–400 (IEEE, 1998).
147. Singh, R. et al. A reconfigurable dual-frequency narrowband CMOS LNA using phase-change RF switches. *IEEE Trans. Microw. Theory Tech.* **65**, 4689–4702 (2017).
148. Razavi, B. & Behzad, R. *RF Microelectronics* Vol. 2 (Prentice Hall, 2012).
149. Ham, D. & Hajimiri, A. Concepts and methods in optimization of integrated LC VCOs. *IEEE J. Solid-State Circuits* **36**, 896–909 (2001).
150. Lu, T.-Y., Yu, C.-Y., Chen, W.-Z. & Wu, C.-Y. Wide tunning range 60 GHz VCO and 40 GHz DCO using single variable inductor. *IEEE Trans. Circuits Syst. I: Regul. Pap.* **60**, 257–267 (2012).
151. Wen, C.-Y. et al. A phase-change via-reconfigurable CMOS LC VCO. *IEEE Trans. Electron. Devices* **60**, 3979–3988 (2013).

Acknowledgements

Author contributions

D.K. and S.J.Y. contributed equally to this paper. D.K., S.J.Y., N.W., S.S., G.D., E.P., H.H., M.K. and D.A. researched data for the Review. D.K., E.Y., M.K. and D.A. contributed substantially to discussion of the content. D.K., S.J.Y., M.K. and D.A. wrote the article. M.K. and D.A. reviewed and/or edited the manuscript before submission.

Competing interests

The authors declare no competing interests.

Additional information

Supplementary information The online version contains supplementary material available at https://doi.org/10.1038/s44287-023-00001-w.

Peer review information *Nature Reviews Electrical Engineering* thanks Han Wang, Mario Lanza and the other, anonymous, reviewer(s) for their contribution to the peer review of this work.

Publisher's note Springer Nature remains neutral with regard to jurisdictional claims in published maps and institutional affiliations.